THE PENNSYLVANIA STATE UNIVERSITY
SCHREYER HONORS COLLEGE

DEPARTMENT OF ASTRONOMY AND ASTROPHYSICS

BLACKCAT SHORT BURST DETECTION EXPECTATIONS VIA PROMPT AND EXTENDED EMISSION SIMULATION

LUKE ROYER
SPRING 2026

A thesis
submitted in partial fulfillment
of the requirements
for baccalaureate degrees
in Astronomy and Astrophysics and Physics
with honors in Astronomy and Astrophysics

Reviewed and approved* by the following:

Derek Fox
Professor of Astronomy and Astrophysics
Thesis Supervisor

William Brandt
Professor of Astronomy and Astrophysics
Honors Adviser

*Signatures are on file in the Schreyer Honors College.

Abstract

Launched in January 2026 and currently undergoing on-orbit validation, Penn State's Black Hole Coded Aperture Telescope (BlackCAT) is a NASA-funded CubeSat (6U) mission dedicated to high-energy transient discovery and wide-sky X-ray monitoring. While BlackCAT's rate of burst detections, and expected redshift distribution, for long-duration gamma-ray bursts (long bursts) have previously been estimated from high-fidelity simulations using prototype flight software, the rate of detections and observed redshift and luminosity distributions for short-duration gamma-ray bursts (short bursts) have not. While expected to account for a distinct minority ($\lesssim$10%) of BlackCAT gamma-ray bursts, the short bursts are of particular scientific interest due to their origins in compact object mergers. Such compact object mergers have the potential to be detected as gravitational wave events, as with the multimessenger transient GW 170817 / GRB 170817A, and have been shown to be important sites of r-process nucleosynthesis. Through modeling of the short burst population, using template burst lightcurves and spectra from the *Swift* BAT catalog, and applying BlackCAT prototype flight software as in previous studies, we explore BlackCAT's sensitivity to short GRBs and derive predicted redshift and luminosity distributions. These are not only the first simulations of short burst detection for BlackCAT but, to our knowledge, the first simulations of the detectability of short bursts by X-ray instrumentation of any sort that explore the detectability of short bursts with and without the extended, softer emission that is observed to accompany a significant fraction of short bursts. We find an expected rate of 2.8 detected bursts per year on-orbit for BlackCAT. Accounting for the extended emission of some short bursts increases detection sensitivity by a factor of $\approx$4, allowing these bursts to be detected to greater distances and lower luminosities.

Table of Contents

List of Figures

List of Tables

Acknowledgements

I am grateful for the opportunity and support offered by the Schreyer Honors College to pursue this thesis. I would like to thank Dr. Derek Fox for his invaluable insight as my honors thesis supervisor, as well as the rest of the BlackCAT science team for their help and input on this project: Dr. Abe Falcone, Dr. Joseph Colosimo, and Tim Emeigh. I would like to thank my advisors Dr. Niel Brandt and Dr. Chris Palma for their guidance in my academic career. This project would not be possible without the constant support from my family and friends.

Chapter 1

Introduction

1.1 Gamma-Ray Bursts

Gamma-ray bursts (GRBs) are defined observationally as brief bursts of hard X-ray to gamma-ray emission from cosmic sources, with durations of milliseconds to minutes (and in the most extreme cases, hours; Levan et al. 2014). The brightest such bursts, occurring at a rate of roughly twice per day over the full sky (Paciesas et al., 1999), outshine the summed emissions of the remainder of the gamma-ray sky when active. GRBs have an isotropic sky distribution and a non-Euclidean flux distribution (Meegan et al., 1992), which was used to argue in favor of their cosmological origins – and extreme luminosities – prior to the identification of the first afterglow and host galaxy (e.g., Paczynski 1992).

Availability of prompt arcminute-scale GRB localizations via the *Beppo-SAX* mission, beginning in 1996 (Boella et al., 1997), rapidly led to the discovery of GRB afterglow emission (Mészáros & Rees, 1997; Costa et al., 1997): long-lived multiwavelength (X-ray to radio) counterparts that rise quickly to a peak and then decay, in piecewise power-law form, over the subsequent hours, days, weeks, and months. GRB afterglows, in turn, enabled precise localizations, host galaxy identifications, and extensive counterpart studies, rapidly confirming their cosmological distances (van Paradijs et al., 1997), yielding the first GRB redshift (Metzger et al., 1997), and ultimately, multiple GRB-associated supernovae including GRB 980425/SN 1998bw (Galama et al., 1998; Kulkarni et al., 1998) and GRB 030329/SN 2003dh (Stanek et al., 2003).

This confirmed the nature of some GRBs as collapsars (MacFadyen & Woosley, 1999): Massive stellar explosions that generate high-luminosity, highly-relativistic (Lorentz factor $\Gamma \gtrsim 100$) jetted outflows while simultaneously exploding as type Ibc supernovae (Woosley & Bloom, 2006).

1.2 The Nature of Short Bursts

However, as noted by observers and theorists at the time, prior to the launch of the *Swift* mission in November 2004, no afterglows, host galaxies, associated supernovae, nor counterparts of any kind had been identified for any short-duration GRBs (hereafter short bursts).

The division of the GRB population into two classes: long-soft and short-hard, or simply "long" and "short," was proposed early on via KONUS Venera data (Mazets et al., 1981), and confirmed with high confidence in the first BATSE catalog (Kouveliotou et al., 1993). Since the *Beppo-SAX*, *Rossi X-ray Timing Explorer* (Swank, 1999), and *HETE-2* (Pizzichini et al., 2004) missions all localized GRBs using coded-aperture X-ray instruments, the shorter durations and harder spectra of the short bursts led to much reduced X-ray fluences by comparison to the long bursts, and hence, very infrequent short burst detections by these facilities.

The launch of *Swift* (Gehrels et al., 2004), along with a bright short burst fortuitously caught by *HETE-2* (Villasenor et al., 2005), finally brought the afterglow revolution to the short burst population in 2005. The first short burst afterglow and host galaxy studies immediately confirmed the contrasting nature of the short burst population (Fox et al., 2005): short burst prompt and afterglow luminosities were lower, and short bursts were often found among old stellar populations and in the outskirts of galaxies; hence, they could not (all) be associated with massive, short-lived stars. Moreover, none of the short bursts exhibited associated supernovae, to deep limits. A consensus thus quickly emerged that short bursts were likely due to compact object mergers – binary neutron star or neutron star + black hole systems, driven to their final coalescence by gravitational radiation, as suggested early on by Eichler et al. (1989); for a review, see Berger (2014).

The *Swift* mission, with its sensitive BAT instrument, automated X-ray and UV/optical follow-up capability, and 20+ year mission lifetime, along with persistent global follow-up campaigns, has since accumulated a significant catalog of short burst afterglow detections, including 79 with redshift measurements from afterglow or host galaxy spectroscopy which will be used in this paper. These observations have clarified the short bursts' luminosity and redshift distributions (e.g., Ghirlanda et al. 2016) and provided extensive support to these fundamental observational distinctions between long and short bursts.

In addition, *Swift* studies have established the presence of "extended emission" in the X-ray band following the prompt emission of some short bursts (Kaneko et al., 2015). This emission rises to a peak following the prompt emission of the burst, lasts for an extended period of seconds to hundreds of seconds, and exhibits a distinct and softer spectrum. The varying properties of bursts with and without extended emission suggests the possibility of distinct progenitors, or progenitor systems, for these two classes of short burst (Troja et al., 2008). For purposes of this project, which seeks to establish detection rates of short bursts, we remain agnostic as to whether the two classes of short burst have distinct origins, simulating both classes and exploring the detectability of each.

1.3 Short Bursts as Gravitational Wave Sources

The compact binary merger model of short bursts promised a unique application for these events: Bursts that occur near enough to Earth, during an active observing run of one or more sensitive gravitational-wave observatories, should be accompanied by a transient gravitational wave (GW) signal. Such binary inspiral + merger events have long served as a key target population motivating the construction and operation of GW facilities, which today include the Laser Interferometer Gravitational Wave Observatory (LIGO; Abbott et al. 2009), the Virgo Interferometer (Virgo; Accadia et al. 2012), and the Kamioka Gravitational Wave Detector (KAGRA; Abe et al. 2022). Models of binary stellar evolution – from binary star formation through the full process of stellar evolution, including two supernovae – and observations of binary neutron star systems in the Galaxy were used to estimate the cosmic rate of compact binary mergers (e.g., Kalogera et al. 2004) and establish the target strain sensitivity of $h \lesssim 10^{-21}$ for these facilities. The strain, $h \equiv \delta\ell/\ell$, characterizes the strength of a gravitational wave at Earth, as the change in length $\delta\ell$ observed over a distance ℓ, where $\ell = 4\,\mathrm{km}$ for the LIGO facilities.

In 2015, during a commissioning period before the start of its first observing run at this target sensitivity, LIGO detected the GW 150914 compact binary merger event, the GW signal of a merging binary black hole system at 440 Mpc distance (Abbott et al., 2016). Since the two merging black holes had masses of 36 $M_{\odot}$ and 29 $M_{\odot}$, respectively, the generated GW signal was much stronger than for a binary neutron star merger; the maximum neutron star mass is likely about 3 $M_\odot$, with typical masses in the range 1.4 $M_\odot$ to 1.8 $M_\odot$. Mergers of massive binary black holes, being detectable to much greater distances than neutron star mergers, do not have to occur at a greater volumetric rate to dominate the event rate for GW facilities. And indeed, over the subsequent months and years, GW events were detected at an increasing rate during LIGO + Virgo observing runs, thanks to steadily improving sensitivities, and consisted almost entirely of binary black hole mergers. Such mergers are not anticipated to yield a bright associated electromagnetic (EM) signal since, in most cases, the black holes merge as purely gravitational objects, without any associated matter or strong EM fields to generate a GRB or other EM-bright counterpart.

At 12:41:04 UTC on 17 August 2017, the LIGO detectors were operating in a nominal state and observed a nearly 30 s long GW inspiral and merger event, GW 170817, consistent with a binary neutron star merger at a distance of 44 Mpc (Abbott et al., 2017a). The masses of the two components of the merger were estimated at 1.3 $M_\odot$ to 2.3 $M_\odot$ and 0.8 $M_\odot$ to 1.4 $M_\odot$, respectively, consistent with one or both objects being neutron stars; bright associated EM emission from this event thus seemed possible. The Virgo detector did not detect the GW signal, but as it was observing in a nominal and sensitive state at the time, its data contributed useful constraints on the direction and polarization of the GW signal.

Roughly 2 s after the merger, the *Fermi* Gamma-ray Burst Monitor (GBM; Meegan et al. 2009) and *INTEGRAL* SPI-ACS (Rau et al., 2005) gamma-ray instruments detected a short burst, GRB 170817A, with a position consistent with the GW localization (Abbott et al., 2017b).

Joint analyses of the GW and EM datasets provided guidance to ground-based observers as to the sky location and distance to the event. One of the most promising known galaxies consistent with these constraints, NGC 4993, was soon observed by astronomers, and a new optical source, SSS17a, identified (Coulter et al., 2017). This proved to be the "kilonova" counterpart to GW 170817, which subsequently manifested as an afterglow visible across the EM spectrum, from radio to X-ray, and became in all likelihood the most-observed transient astronomical source since SN 1987A (Margutti & Chornock, 2021).

This singular transient, the first GW+EM multimessenger event, thus provided dramatic confirmation of the compact binary merger model for the short bursts. Moreover, an enormous range of scientific insights followed from the merger detection and subsequent follow-up observations (for a review, see Margutti & Chornock 2021); to summarize, briefly and incompletely:

- The early optical emission was observed to consist of two "kilonovae" – nuclear decay-powered subrelativistic outflows (Metzger, 2020) – one fast and hot (a blue kilonova), and the other slower and cooler (a red kilonova), demonstrating that binary neutron star mergers are important sites of heavy element production – specifically, sites of r-process (rapid, neutron-rich) nucleosynthesis (Evans et al., 2017; Siegel, 2019);

- The short burst was found to have been observed off-axis, consistent with its very low luminosity – it exhibited an average flux, but was by far the nearest short burst ever seen. The rise and decay of its afterglow emissions thus tested the jetted afterglow model of GRBs in a unique and valuable regime (Margutti et al., 2017; Lamb et al., 2019);

- Analyses of the GW data provided constraints on the radii, masses, and tidal deformabilities of the two neutron stars, and hence, the structure of neutron stars and properties of their ultradense interiors – or as the topic is also known – the neutron star equation of state (Abbott et al., 2018);

- Measurement of the GW strain at Earth, combined with the known recession velocity of the host galaxy NGC 4993, provided a direct estimate of the Hubble constant, free of cosmological model assumptions (apart from the galaxy's peculiar velocity) and independent of other astronomical measurements (Abbott et al., 2021);

- The speed of GW propagation – the speed of gravity – was constrained to be very near the speed of light, as otherwise the two signals would not have been coincident at Earth.

The fantastic harvest of scientific insights from GW 170817, and the promise of future such multimessenger detections, thus centers on: (1) Physical characterization of the prompt event, yielding insights into the properties of ultradense matter, General Relativity and strong field gravity, and the formation of jets and outflows from compact binary mergers, including off-axis properties of these phenomena; (2) Observational studies of kilonova outflows, which promise insights into r-process nucleosynthesis and the properties of neutron-rich high-Z isotopes; and (3) Astrophysical applications of the events, which pinpoint the locations and environments of compact object mergers as well as (individually!) giving direct estimates of the cosmic expansion rate or Hubble constant.

1.4 The BlackCAT CubeSat

Launched January 11, 2026, the Black Hole Coded Aperture Telescope (BlackCAT) is a 6U CubeSat mission. The onboard science instrument is a 15.8 cm focal length coded-aperture telescope utilizing 4 Speedster-EXD550 hybrid CMOS detectors placed in an array. The coded aperture is constructed with gold-plated nickel, consisting of an array of elements in the open (no metal) or closed (17 μm of nickel and 8 μm of gold) state. Approximately half of the elements are in the closed state, placed in a randomly generated pattern. The closed elements can attenuate X-rays below ~ 20 keV. The detectors will be sensitive to soft X-rays between $5 - 20$ keV. Images formed through the coded aperture indicate the direction of the photons' travel, increasing positional accuracy. This construction produces an effective field of view (FOV) of 0.85 steradians with an estimated positional accuracy of $40''$ to $55''$. A summary of important mission parameters is presented in Table 1.1 (Colosimo et al., 2024).

Mission Parameter	Value
Platform	6U CubeSat
Energy Band	0.5-20 keV
Effective Area (at 5 keV)	7.7 cm^2
Field of View	0.85 sr
Source Localization	$40''$ to $55''$
Duty Cycle	$\sim 76\%$

Table 1.1: A collection of expected mission parameters for the BlackCAT CubeSat mission (Colosimo et al., 2024). The field of view is reported for the partially coded mask.

BlackCAT has been launched into a dawn-dusk Sun-synchronous low-Earth orbit. This provides thermal stability and near-continuous solar power, while allowing ready access to the night-time sky. The main disadvantage of the orbit is regular passage through regions of low geomagnetic rigidity near the magnetic poles and South Atlantic Anomaly, during which high charged particle backgrounds prevent high-sensitivity X-ray observations. BlackCAT plans to maintain a mostly anti-Sun pointing, enabling transient discovery and X-ray source monitoring over a significant fraction of the night-time sky for ground-based observers. The satellite will observe using stepwise stares, alternating slews and fixed pointings, to accommodate Earth-limb and thermal management pointing constraints; effective observation time on-orbit is also affected by these slews. The on-orbit duty cycle, after excluding active slews and portions of the orbit affected by high particle backgrounds, is estimated to be 76% (Colosimo et al., 2024).

1.5 Goals

BlackCAT is designed as a wide-sky X-ray monitor and high-energy transient discovery mission. Its primary scientific objective is to discover GRBs from high redshift ($z \gtrsim 3.5$) and provide prompt sub-arcminute positions for follow-up observations. Since long bursts are more energetic than short bursts, and since BlackCAT offers a relatively soft bandpass compared to the *Swift* BAT (0.5–20 keV vs. 15–150 keV), we expect the relative fraction of short bursts to be reduced below the ≈10% fraction observed in the BAT sample. As with the *Swift* sample, we also expect the short burst fraction to decline toward higher redshifts, $z > 3.5$.

Nonetheless, BlackCAT short burst studies promise to be of scientific value, for several reasons:

- The nearest short bursts, those that will be detected as GW events from $D \lesssim 120$ Mpc, have the potential to be very bright, and thus easily detected.
- We have previously estimated that GW 170817 / GRB 170817A, a short burst with extended emission which was not very bright due to being observed off-axis, could nonetheless have been recovered at $\approx 3.5\sigma$ significance in ground analysis of BlackCAT data.

- The presence of softer extended emission episodes in many *Swift* BAT short bursts encourages us to evaluate the X-ray detectability of short bursts with extended emission, which has not previously been done.

- All short bursts detected by BlackCAT, no matter their distance or redshift, will be located in the night sky and localized to $\lesssim 1'$ precision in real time, with alerts provided to follow-up observers. They therefore promise to be fruitful targets for follow-up observations.

Follow-up studies of short bursts at $z \gtrsim 0.03$ are useful for understanding the burst afterglows and jets, their host galaxies and subgalactic environments, and their redshift and luminosity distributions. Short bursts at $z \lesssim 0.5$ can be studied in detail with *JWST* to search for and characterize any kilonova emission, and associated signatures of r-process nucleosynthesis.

In this paper, we aim to test BlackCAT's sensitivity to short bursts, and estimate the rate of short burst detections along with their luminosities and redshifts. Drawing on theoretical studies of the burst population, we create a model of the short burst population. Sampling from our model, we aim to determine the observed distributions and the predicted rate of detected short bursts. Using *Swift* BAT template light curves and spectra for each simulated burst, we execute the flight software trigger for the BlackCAT instrument to determine the observed significance of the event. We then analyze the complete set of detected short bursts to derive the expected detection rate and redshift and luminosity distributions for BlackCAT. Finally, by simulating the prompt and extended emission of short bursts with extended emission separately, as well as together, we are able to characterize BlackCAT performance with respect to these features.

Chapter 2

Burst Properties and Populations

2.1 Swift Burst Properties

To accurately capture the behavior of real-world short GRBs, our simulations are derived from events observed by the *Swift* BAT instrument. For simulation purposes, a burst's distance is chosen via its cosmological redshift. Since this is an important aspect of our rescaling method, only bursts with a well-defined redshift are chosen. A catalog of 79 bursts is selected as templates. Table 2.2 summarizes the burst properties described below.

For each burst, several parameters are required for their use in random light curve generation. The output light curve of BAT analysis is used as a template for rescaling. We use the flux light curve assuming a non-evolving spectral behavior. In order to ensure that we use statistically significant data, the cutoff signal-to-noise ratio is SNR $= 5$.

The start and stop times for each light curve are taken to be the range where "good" bins - as defined by the *Swift* Burst Analyser (Gehrels et al., 2004) - are found. In some cases, a burst occurred with extended emission. In these situations, the start, cut, and stop times needed to be determined. As an initial guess, the split between prompt and extended emission was taken to be where the time bin lengths become > 2 seconds, to a maximum of $t_{cut} = 2$ seconds. These were checked visually and adjusted manually where necessary. Figure 2.1 illustrates an example burst and its time values.

In addition to the light curve, each burst requires spectral fits. Because of the differing spectral behavior between the prompt and extended emission, these are modeled separately. We model the prompt emission as a cutoff power-law:

$$N_p(E) = N_0 \left(\frac{E}{E_0}\right)^{-\alpha} e^{-E/E_{\rm cut}}, \tag{2.1}$$

where E_0 is the pivot energy, α is the power-law index, $E_{\rm cut}$ is the cutoff energy, and N_0 is a normalization factor. When available, spectral parameters for the burst prompt spectra are taken from existing literature. Since we are using a nonstandard temporal window, however, we determine the

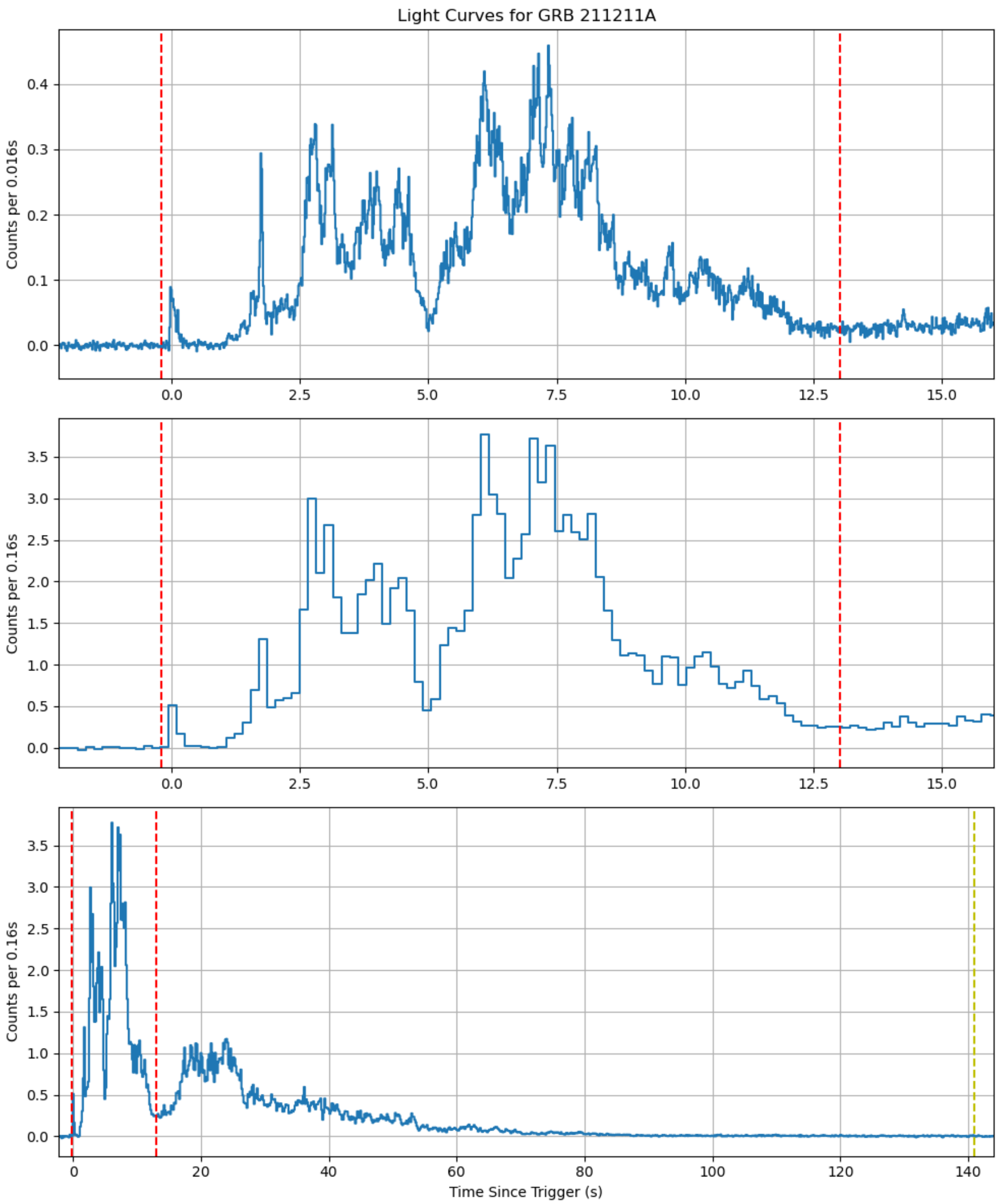

Figure 2.1: An example of light curve timing values t_{start}, t_{cut}, and t_{end}. Shown is the mask-weighted event light curve for GRB 211211A. Top: Prompt emission binned to $\Delta t = 0.016$ seconds with t_{start} and t_{cut} indicated by red vertical dashed lines. Middle: Prompt emission binned to $\Delta t = 0.16$ seconds with t_{start} and t_{cut} indicated by red vertical dashed lines. Bottom: The total light curve binned to $\Delta t = 0.16$ seconds with t_{start} and t_{cut} indicated by red vertical dashed lines and t_{end} indicated by a vertical yellow dashed line.

spectral normalizations directly using Xspec[1]. In cases when a cutoff power-law fit is not found in the literature, we find a 90%-confidence lower-limit on the cutoff energy via χ^2 analysis of the BAT data. The BAT burst spectrum is binned to a minimum of 5 counts per channel above background, a best-fit cutoff power-law model is determined, and the steppar procedure is used to tabulate the variation in χ^2 versus $E_{\rm cut}$, with $E_{\rm cut}$ fixed and the other spectral parameters (normalization and power-law index) free to vary at each step. The 90%-confidence lower-bound on $E_{\rm cut}$ is then determined by interpolation as the value that results in a constrained χ^2 that is $\Delta\chi^2 = 2.3$ above the best-fit (minimum) value.

In the case that a burst has extended emission, we fit the extracted extended emission spectrum over the appropriate temporal interval with a simple power-law:

$$N_e(E) \propto \left(\frac{E}{E_0}\right)^{-\beta}, \tag{2.2}$$

with β set to the time-averaged BAT index after the cutoff time, as determined by the *Swift* Burst Analyzer.

Each burst's bolometric luminosity was found by integrating the prompt emission spectrum between 1 keV and 10^4 keV, corrected for cosmological redshift. For bursts without spectral fits from the literature, the cutoff energy used was the median of the energy distribution function (Eq. 2.4) above the 90%-confidence lower limit. Note that the spectral cutoff energy is related to the observed peak energy $E_p = E_{\rm cut}(2-\alpha)$.

2.2 Short Burst Populations

Following the model of Ghirlanda et al. (2016), we use a flat ΛCDM cosmology where $H_0 = 70\,{\rm km\ s^{-1}\ Mpc^{-1}}$ and $\Omega_m = 0.3$. We consider the results from their case with no correlations and no minimum luminosity. They find a parameterized redshift distribution of short GRBs

[1] Xspec webpage: https://heasarc.gsfc.nasa.gov/docs/software/xspec/index.html

$$\Psi(z) = \Psi_0 \frac{1 + p_1 z}{1 + (z/z_p)^{p_2}} \tag{2.3}$$

This follows a time-delayed cosmic star formation rate, accurately representing the time necessary for merger events to occur. The normalization is taken to be $\Psi_0 = 0.20 \pm 0.05$ Gpc^{-3} yr^{-1} consistent with their results. We opt to work with the observable peak energy E_p. In their paper, Ghirlanda et al. (2016) assume a broken power law form of the probability distribution:

$$\phi(E_p) \propto \begin{cases} (E_p/E_{p,b})^{-a_1}, & E_p \leq E_{p,b}; \\ (E_p/E_{p,b})^{-a_2}, & E_p > E_{p,b}. \end{cases} \tag{2.4}$$

There exists a correlation between the peak energy and the total luminosity of the burst. The adopted E_p–L relation is:

$$\log_{10}(E_p/670\,\mathrm{keV}) = q_Y + m_Y \log_{10}(L/10^{52}\,\mathrm{erg\ s^{-1}}). \tag{2.5}$$

Table 2.1 gives the reported parameters for the Ghirlanda et al. (2016) SGRB population models.

Parameter	**Mean Value**	**68% C.I.**
a_1	0.53	$(0.2, 1)$
a_2	4	$(1.9, 4.4)$
$E_{p,b}$	1600	$(880, 2000)$
m_Y	0.84	$(0.58, 0.88)$
q_Y	0.034	$(-0.069, 0.18)$
p_1	2.8	$(0.59, 3.7)$
p_2	3.5	$(0.94, 4)$
z_p	2.3	$(1.7, 3.2)$

Table 2.1: Short Gamma Ray Burst population parameters as defined by Ghirlanda et al. (2016) Provided are the mean value and the 68% Confidence Interval.

In their paper, Ghirlanda et al. (2016) discuss detectable SGRB rates for the local universe. The following procedure replicates these results; however, as we are simulating the full-universe rate, we need to integrate their distribution out to a much higher redshift ($z = 30$). To do so, we adopt the cosmological equations laid out in Wright (2006). The cosmological volume integral is:

$$V(< z) = 4\pi R_0^3 \int_0^{\psi} \frac{1 - \cos 2\psi'}{2} d\psi' \tag{2.6}$$

where $\psi = \sqrt{|1 - \Omega_{\text{tot}}|} Z(z)$, $R_0 = (c/H_0)/\sqrt{|1 - \Omega_{\text{tot}}|}$, and $Z(z)$ is the comoving distance divided by the Hubble radius (c/H_0):

$$Z(z) = \int_0^z \frac{dz}{(1 + z)\sqrt{X}}. \tag{2.7}$$

The function X is defined by:

$$X = \Omega_m (1 + z) + \Omega_r (1 + z)^2 + \Omega_\Lambda/(1 + z)^2 + (1 - \Omega_{\text{tot}}), \tag{2.8}$$

with $\Omega_\Lambda = 0.7$, $\Omega_r = 4.165 \times 10^{-5}/h^2$, and $h = H_0/100$ km s^{-1} Mpc^{-1}. To avoid numerical instabilities, we use $\Omega_{\text{tot}} = 0.99$.

Computing Z for every step of the volume integration would be unnecessarily taxing on computational resources. Instead, we opt to compute Z at integer steps from $z = 0$ to $z = 31$ and utilize a cubic spline interpolation. In addition, Eq. 2.3 is in terms of z while the integration is with respect to ψ. To account for this, the inverse function of ψ was used: $z(\psi) = \psi^{-1}(\psi) = Z^{-1}(\psi/\sqrt{|1 - \Omega_{tot}|})$. Again, a cubic spline interpolation is used to find the inverse function Z^{-1}.

The final integration is then:

$$\rho_0 = 4\pi R_0^3 \Psi_0 \int_0^{\psi} \frac{1 + p_1 z(\psi')}{1 + (z(\psi')/z_p)^{p_2}} \times \frac{1}{1 + z(\psi')} \times \frac{1 - \cos 2\psi'}{2} d\psi' \tag{2.9}$$

Note the extra term of $(1+z)^{-1}$ accounts for the cosmological correction to the redshift distribution. Integrating out to $z = 30$ gives a rate of $\rho_0 = 365 \pm 19$ yr^{-1}. In the 0.85 steradian field of view of

BlackCAT, we therefore expect 24.7 ± 1.3 detectable bursts per year to occur.

2.3 Burst Parameter Table

Table 2.2 presents the observed and derived parameters for the short bursts used as templates in our simulations.

GRB	$t_{\rm start}$	$t_{\rm cut}$	$t_{\rm end}$	z	$\log L$	E_p	N_0	α	β	Note	Ref.
231117A	−0.384		1.256	0.257	53.255	400	13.422	1.15		f	1
211211A	−0.192	13.008	140.968	0.0763	52.496	646.8	22.420	1.30	1.55	a,f	2
211023B	−0.436		1.644	0.862	51.316	>52	0.032	1.34			
210919A	0.048	0.388	283.648	0.2415	52.207	73	6.870	1.08	3.22	g	3
210726A	−0.076		2.000	0.37	50.168	41	0.282	0.23		f	4
210323A	−0.204	0.496	721.936	0.733	53.721	1826	0.661	0.89	2.66		5
201221D	−0.140		0.260	1.045	52.139	108	0.397	0.20			6
200907B	−0.488		0.272	0.56	51.508	>164	0.103	0.46		b	
200522A	−0.044		0.616	0.554	51.490	78	0.443	0.54			7
200411A	−0.108		0.392	0.7	52.793	420	0.432	0.64		a	8
200219A	−0.280	0.590	307.800	0.48	51.147	1387	0.005	0.65	1.79		9
191031D	−0.076	0.324	320.944	0.5	53.040	856	0.554	0.42	1.06		10
181123B	−0.044	0.414	40.344	1.754	53.113	>127	0.232	0.43	0.71	a	
180805B	−0.216	0.704	157.264	0.661	50.727	346	0.006	0.50	2.08		11
180727A	−0.056		1.264	2	52.042	67.6	0.076	0.59			12
180618A	−0.096	2.216	57.216	0.544	52.031	2290	0.014	0.63	2.22	a	13
180418A	0.004		2.664	1.55	54.055	329	1.278	1.20			14
170728B	−0.180	0.900	40.640	1.27	53.066	160	0.417	1.13	−0.74	a	15
170428A	0.144		0.504	0.45	53.292	1134	0.918	0.53			16
170127B	−0.060	0.440	842.120	2.2	54.061	688	0.249	0.67	2.98		17
161104A	−0.124		0.096	0.79	52.251	>72	1.902	0.80		a,c,e	
161001A	−0.268	2.232	44.452	0.67	52.244	437	0.127	0.46	1.39	a	18
160821B	−0.008		0.392	0.16	49.237	46.3	0.229	0.11			19
160624A	−0.160		2.000	0.483	52.022	800	0.063	0.40		a	20
160525B	−0.018	0.352	560.912	0.64	50.837	>8	11.470	1.73	2.21	c	

GRB	$t_{\rm start}$	$t_{\rm cut}$	$t_{\rm end}$	z	$\log L$	E_p	N_0	α	β	Note	Ref.
160411A	−0.152	0.608	160.928	0.82	51.451	161	0.104	−0.26	0.65	a	21
160410A	−0.060	2.800	82.800	1.717	52.407	1416	0.004	0.71	2.64		22
160408A	−0.052	0.518	121.328	1.9	54.593	914	0.901	0.76	4.10		23
160303A	−0.104	0.416	40.456	1	51.953	>101	0.202	0.63	4.27		
151229A	−0.204		2.296	1.4	54.038	97.1	4.293	1.19			24
150831A	−0.068	1.032	81.112	1.18	53.275	564	0.231	0.50	1.81		25
150728A	−0.060	1.008	841.848	0.46	50.046	>1	9.887	1.96	1.12	a,b	
150423A	−0.046		0.224	1.394	52.478	>65	0.507	0.71			
150120A	−0.428	1.032	40.872	0.46	53.095	130	4.123	1.43	3.48		26
141212A	−0.034		0.146	0.596	52.705	>70	0.347	0.14		a,c	
140930B	−0.200		1.100	1.465	54.255	1302	0.427	0.60		a	27
140903A	−0.040		0.340	0.35	50.890	>7	87.819	1.87			
140622A	−0.308		0.332	0.959	55.305	44	87.819	1.74		a,g	28
140129B	0.176	1.216	281.496	0.43	50.316	>50	40.372	2.24	3.62	b	
131004A	−0.240		1.120	0.717	51.357	>18	25.904	1.72		c	
130822A	−0.012		0.078	0.154	50.601	>65	1.968	0.80		a,c,e	
130716A	−0.056	0.424	80.584	2.2	53.254	635	0.035	0.23	1.21	d	29
130603B	−0.048		0.272	0.3564	53.487	894.96	4.134	0.73		a	43
130515A	−0.036	0.284	721.724	0.8	51.893	410	0.039	0	1.61		30
121226A	−0.240	0.560	280.840	1.27	51.797	>56	2.700	1.31	3.07		
120804A	−0.176	1.784	41.784	1	53.656	135	4.610	0.89	1.96		31
120630A	−0.200		0.900	0.6	50.932	>36	0.652	1.03		a	
120305A	−0.058		0.132	0.225	51.492	>88	3.250	0.68		a	
111117A	0.016		0.556	2.211	53.517	440	0.123	0.39		a	32
110402A	2.280	4.920	117.320	0.854	53.651	1025	0.941	1.29	2.17		33
101224A	−0.046	0.304	641.584	0.4536	52.468	330	0.774	0.83	1.16		34
101219A	−0.036		1.164	0.718	51.906	490	0.039	0.22			35
100816A	−0.400	1.680	537.640	0.8035	53.190	148	2.155	1.00	1.81		36
100625A	−0.094	0.336	40.456	0.452	50.188	509.2	0.002	0.64	3.59		37
100206A	−0.050	0.120	761.640	0.4068	52.031	506	0.189	0.18	3.29	a	38
100117A	0.016	0.296	631.496	0.92	48.951	287	0.000	0.14	1.74		39
090515A	−0.060	0.052	481.012	0.403	52.017	>41	6.357	0.80	2.12	a,c,e	

GRB	$t_{\rm start}$	$t_{\rm cut}$	$t_{\rm end}$	z	$\log L$	E_p	N_0	α	β	Note	Ref.
090510A	−0.016	0.344	280.904	0.903	53.667	3990	0.116	0.66	2.38	f	40
090426A	−0.064		0.976	2.609	54.264	176.84	1.177	1.00		f	43
080905A	0.032		0.512	0.1218	49.939	578.95	0.018	0.13			43
080123A	−0.004	0.676	120.796	0.495	52.962	104.65	4.291	1.20	2.85	c	43
071227A	−0.644	1.736	281.736	0.383	50.707	>112	0.287	0.80	2.56	a,e	
070809A	−0.100	1.040	801.760	0.2187	49.752	>10	5.084	1.52	3.32	a	
070729A	−0.168	1.128	401.928	0.52	51.139	>45	0.084	0.47	2.66	a	
070724A	−0.100	0.530	481.320	0.457	50.760	>19	3.849	1.33	4.27	a	
070714B	−0.792	1.288	90.288	0.92	52.765	2150.4	0.035	0.86	2.90		43
070429B	−0.308	0.312	721.752	0.904	51.666	>13	5.622	1.31	1.18	a	
061217A	−0.144	0.244	721.664	0.827	51.951	>56	0.112	0.40	1.92	a,c	
061210A	−0.050	0.070	102.720	0.4095	52.241	>106	5.240	0.71	1.98	a	
061201A	−0.028	0.892	161.052	0.111	50.194	>153	0.386	0.58	1.37		
061006A	−23.240	−21.240	111.720	0.4377	51.313	>203	0.884	0.84	2.27		
060801A	0.028		1.988	1.131	52.000	>80	0.226	0.68		c	
060614	−2.320	−0.320	214.960	0.125	52.254	302	6.141	1.57	2.27		41
060502B	−0.024		0.126	0.287	51.076	>40	2.003	0.84		c	
051227A	0.032	1.952	133.232	0.8	51.088	>77	0.326	0.99	1.92	b	
051221A	−0.056		1.864	0.5465	53.516	402	4.225	1.08			42
051210A	−1.264		2.000	2.5	52.320	>49	0.178	0.84		a	
050724A	−0.160	0.920	155.720	0.258	50.531	>36	5.434	1.25	2.23	a	
050509B	−0.060		0.048	0.226	50.848	>92	1.375	0.80		a,c,e	

GRB	$t_{\rm start}$	$t_{\rm cut}$	$t_{\rm end}$	z	$\log L$	E_p	N_0	α	β	Note	Ref.

Table 2.2: Observed and derived parameters of short bursts in our catalog. Burst start, cut, and end times $t_{\rm start}$, $t_{\rm cut}$, and $t_{\rm end}$ are in seconds relative to the BAT burst trigger time; log luminosities $\log L$ are in erg s^{-1} over the restframe bandpass of 1 keV to 10^4 keV; spectral peak energies E_p are in keV. Literature pivot energies use $E_0 = 100$ keV while fits made with `Xspec` use $E_0 = 1$ keV.

Table Notes: [a]Automated burst analysis results as to start, cut, and stop times were considered suboptimal, and corrected by manual analysis. Spectral analyses were then carried out using the revised time intervals. [b]The automated peak energy minimization failed to find a fit due to the fit being insensitive to a parameter, causing the Monte Carlo Markov Chain to proceed too slowly. The gaussian deltas were adjusted by a factor of 100 to allow the chain to find a fit in sufficient time. [c]The automated peak energy minimization failed to find a satisfactory χ^2 value due to a nonlinearity in the `steppar` data. These bursts showed a global minimum in the `steppar` data, which we adopt as a lower limit on E_p. [d]The automated peak energy minimization failed to find a satisfactory χ^2 value due to a nonlinearity in the `steppar` data. No clear minimum was present, so the data were interpolated over the nonlinearity to find the appropriate critical χ^2 and lower limit on E_p. [e]The best fit parameter for the prompt emission index was found to be $\alpha > 2$, which gives a nonphysical (negative) E_p. We fix the power-law spectral index of the prompt emission at $\alpha = 0.8$ before proceeding with our analysis. [f] Literature peak energies were reported alongside a Band spectral fit. As peak energies are observable, we adopt a cutoff power law with the spectral index equal to the low-energy Band index. In the BlackCAT band, this is sufficiently accurate. [g] Only an an observed peak energy is reported without a corresponding fit. `Xspec` is used with E_p fixed to find the remaining fit parameters.

Table References: [1]Svinkin et al. (2023); [2]Mangan et al. (2021); [3]Minaev et al. (2022); [4]Veres & Fermi-GBM Team (2021); [5]Shan et al. (2024); [6]Hamburg et al. (2020); [7]Fong et al. (2021); [8]Bissaldi et al. (2020); [9] Lü et al. (2020); [10]Mailyan et al. (2019); [11]Hamburg et al. (2018); [12]Lien et al. (2018); [13]Jordana-Mitjans et al. (2022); [14]Rouco Escorial et al. (2021); [15]Kozlova et al. (2017); [16]Tsvetkova et al. (2017); [17]Veres & Meegan (2017); [18]Frederiks et al. (2016a); [19]Acciari et al. (2021); [20]O'Connor et al. (2021); [21]Roberts & Hui (2016); [22]Frederiks et al. (2016b); [23]Roberts (2016); [24]von Kienlin & Meegan (2015); [25]Golenetskii et al. (2015); [26]von Kienlin & Burns (2015); [27]Golenetskii et al. (2014); [28]Sakamoto et al. (2014); [29]Foley & Meegan (2013); [30]Golenetskii et al. (2013); [31]Berger et al. (2013); [32]Sakamoto et al. (2013); [33]Bhat (2011); [34]McBreen (2010); [35]Golenetskii et al. (2010a); [36]Golenetskii et al. (2010b); [37]Bhat (2010); [38]von Kienlin (2010); [39]Paciesas (2010); [40]Leonov et al. (2022); [41]Yang et al. (2022); [42]Jin et al. (2007); [43]D'Avanzo et al. (2014)

Chapter 3

Simulation Methods

3.1 Peak Energy Sampling

As discussed in the previous chapter, there were cases in which a burst did not have a recorded prompt spectral fit with a cutoff power-law form. In these cases, we derived 90% confidence lower limits on the peak energy. Each time one of these bursts was called during the simulation, a new peak energy was selected from the assumed probability distribution (see Equation 2.4) via the inverse cumulative distribution function. The 90% confidence lower limit was used as the lower bound of the random selection.

Choosing the peak energy from the observed distribution ensures that the simulated collection of this case accurately represents the true population of short GRBs. The maximum sampled peak energy is set to 10^5 keV, ensuring that no nonphysical models are being selected from the tail of the distribution function. This process has the added benefit of producing further variety in the population of simulated bursts while obeying physical constraints.

3.2 Light Curve Generation

We follow the simulation methods laid out in Colosimo et al. (2024) For each simulated burst, a random luminosity and redshift are chosen from their respective distribution functions. The redshift is pulled directly from the time-delayed cosmic star formation rate $\Psi(z)$ (Equation 2.3). To find a luminosity, a random peak energy is chosen from the assumed probability distribution $\phi(E_p)$ (Equation 2.4) and a luminosity is found from the $E_p - L$ correlation (Equation 2.5). Random values are taken between $0 < z < 30$ and $0.1\,\text{keV} < E_p < 10^5\,\text{keV}$.

Once the $E_p - L$ correlation is evaluated, a template burst is selected from among the 10 catalog bursts with the closest luminosities. Selecting from a nearby luminosity ensures that the burst's temporal shape sufficiently matches with the energy output. If the burst has an extended emission, the burst's light curve is split into two curves at the cut time. In the case that the template burst does not have a literature cutoff power-law spectral fit, the peak energy is randomized, as discussed in Sec. 3.1.

The light curve's temporal components are scaled by the redshift factor $(1 + z_{new})/(1 + z)$, accounting for cosmological time dilation. The flux is scaled to the new luminosity (L_{new}/L), the new cosmological luminosity distance $(D_L/D_{L,new})$, and a normalization factor corresponding to the bandpass K-correction. The K-correction is found by integrating the prompt spectrum over the standard BAT bandpass $(15 - 50$ keV$)$ and the redshift-scaled bandpass $(1 + z_{new})/(1 + z) \times (15 - 50$ keV$)$. For consistency, we assume a standard flat ΛCDM cosmology (see Section 2.2).

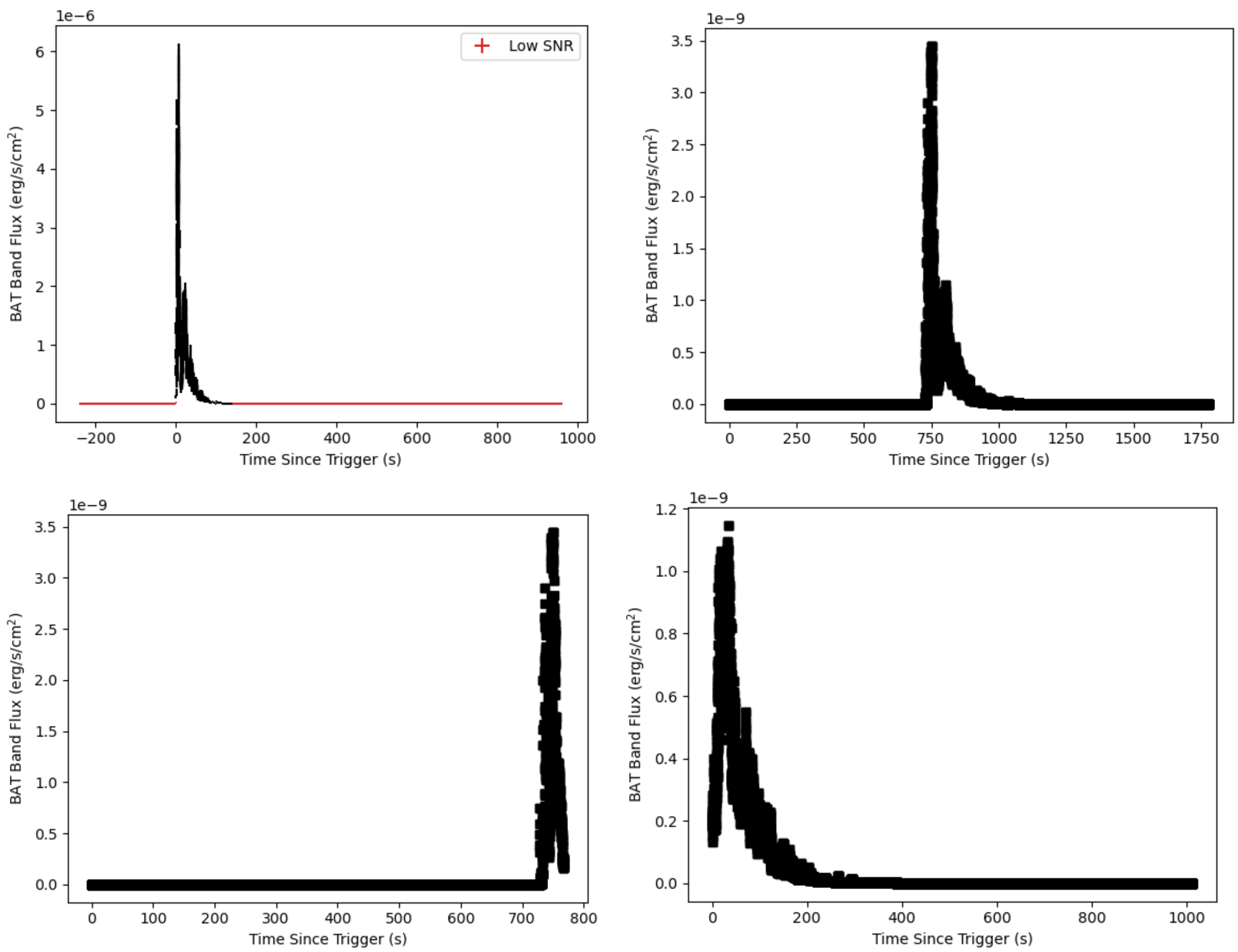

Figure 3.1: An example of a simulated light curve. The initial parameters are $\log L = 52.495$ and $z = 0.0763$. The new parameters are $\log L_{new} = 52.394$ and $z_{new} = 2.269$. Top Left: The template burst GRB Top Right: The scaled simulated total light curve. Bottom Left: The scaled simulated prompt emission light curve. Bottom Right: The scaled simulated extended emission light curve.

In addition to the light curve, the prompt spectra are rescaled. The peak energy is scaled by the redshift factor, accounting for time dilation. The power-law spectra have no factors that scale with new luminosity or redshift, so the extended spectra remain unchanged.

The scaled spectra are used to find the flux conversion factors in the BlackCAT detection bandpasses. This is done by comparing the integrated detection bandpass to the BAT bandpass of the appropriate spectrum. For the case with no extended emission, there is one output light curve and set of flux conversion factors. For the case with extended emission, there were three outputs: prompt only, extended only, and the total light curve.

3.3 Burst Detection Simulations

Each simulated light curve was run through prototype flight software to mimic the detection methods of the BlackCAT instrument. To have the highest chance of flagging a detection, we consider a large number of triggers spanning a variety of timescales and energy ranges. For each event, 70 total triggers are run, covering 10 timescales between 0.125 and 64 seconds and 7 energy bands within the $0.5 - 20$ keV sensitivity range of BlackCAT.

The bursts are uniformly distributed across the 0.85 sr field of view of BlackCAT. For each trigger, we use the simulated burst's light curve as the template to test the response. The light curve is sampled to the corresponding time interval, and the photon flux is rescaled to the trigger's energy range using the spectral model. In the case that the light curve has an extended emission, the prompt photons are sampled with the cutoff power-law spectrum while the extended photons are sampled with the simple power-law spectrum.

With burst photons have sampled, the cosmic X-Ray background is modeled as a broken power-law spectrum. The model is taken from Comastri et al. (1995) and Moretti et al. (2009). Background photons are sampled within the trigger's energy range.

A burst must fulfill several requirements to be considered a successful detection.

1. In the full-detector light curve, we require the burst to have at least 10 successfully detected counts. This sets a minimum significance of the burst's light curve.

2. Both the burst photons and background photons are used to simulate pixel counts. This is done by deconvolving the counts onto the detector via the mask pattern. The deconvolution produces a sky image for each trigger. Within the images, peaks are identified with a minimum image significance of 4.5σ.

3. The reconstructed image position of the burst must match – within a tolerance of 1° – the input position that was randomly selected when the bursts were uniformly distributed across the detector FOV.

4. The burst must be the most significant candidate peak in the field of view. We flag the detection in the case that the burst is dominated by a background fluctuation.

The MAXI Solid-state Slit Camera (SSC) all-sky X-ray maps (Nakahira et al., 2020) are used to simulate X-ray point sources and diffuse emission. Random pointings are taken from the predicted BlackCAT flight path. For each pointing, the MAXI background count rate within the bandpass of the trigger is determined. The significance is scaled by the square root of the original assumed background rate to the MAXI measured rate:

$$\kappa' = \kappa \sqrt{\frac{B_i}{B_{\mathrm{MAXI}}}} \tag{3.1}$$

where κ' is the corrected significance, κ is the initial significance, B_i is the initial background rate, and B_{MAXI} is the point-source background rate. Burst detections are considered successful to be when the aforementioned conditions are met and the point-source corrected significance $\kappa' > 6.5$.

Chapter 4

Results and Discussion

4.1 Simulation Results

We simulate a short burst population appropriate to 100 years of exposure for the BlackCAT coded-aperture instrument, so that the resulting per-year burst rate estimates will be effectively free of Poisson uncertainties. To quote results in terms of time on-orbit, we correct the simulation-derived detection rates for the anticipated 76% duty cycle (Sec. 1.4) of BlackCAT due to active slewing and time spent in high particle-background portions of the orbit. This represents a conservative approach, since the detectors and burst-detection software will operate continuously, and it will remain possible for the spacecraft to detect particularly bright bursts during these periods.

For the full 100-year simulation, we find that a total of 113 prompt-only bursts are detected and 257 bursts with extended emission are detected. Over the duty-cycle corrected 100-year simulation, we get a corrected detection rate of 2.8 short gamma-ray bursts per year. The rate is lower than the predicted long burst detection rate of 41.7 or 43.0 bursts per year for the weak and strong evolution cases, respectively, of Colosimo et al. (2024). This is expected, as mentioned previously, due to the $\approx$10% fraction of short bursts in the *Swift* BAT catalog, and the softer bandpass of BlackCAT. Over the expected lifetime of BlackCAT, this rate will produce a useful collection of bursts for astrophysical studies.

4.2 Observed Redshift Distribution

It is of interest to investigate the expected redshift distribution of detected short gamma-ray bursts. As described in Sec. 2.2, the simulated population of detectable short bursts followed a redshift distribution derived from a time-delayed cosmic star formation rate. By definition, our simulations use observed events as the basis for light curve generation. Deriving our distribution from theoretical models reduces the impact of observational biases.

Redshift	Detection Rate
$z > 0$	2.81 yr^{-1}
$z > 3.5$	0.20 yr^{-1}
$z > 4.5$	0.08 yr^{-1}
$z > 6$	0.02 yr^{-1}

Table 4.1: A collection of selected cumulative burst detection rates at given threshold redshifts. Rates are reported for all bursts detected beyond the indicated z.

As one of BlackCAT's main science goals, we investigate the instrument's high-redshift universe ($z \gtrsim 3.5$) sensitivity for gamma-ray burst events. Figure 4.1 shows the expected cumulative rate for bursts above a redshift z. Table 4.1 provides selected values for the rates above threshold redshifts.

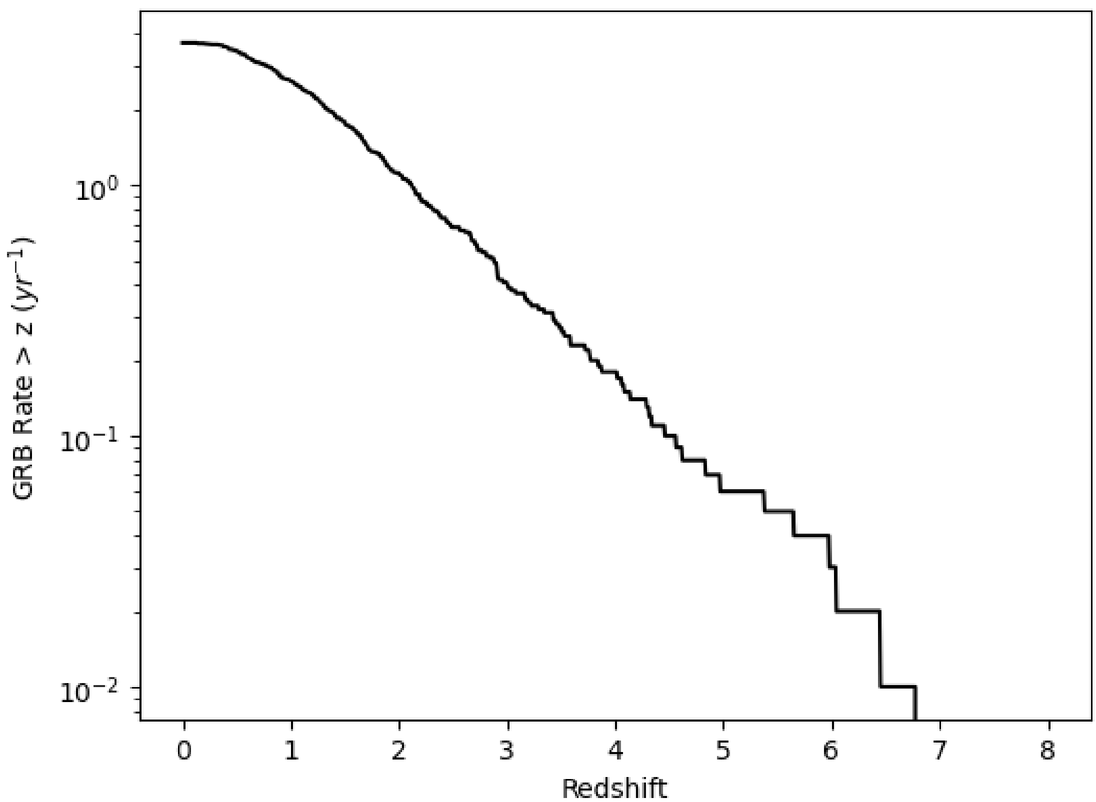

Figure 4.1: Shown is the cumulative detection rate above the threshold z for the full simulation population.

Based on our simulation's successful triggers, we expect that BlackCAT should be sensitive to events in the high-redshift universe. The information provided by these distant bursts will be critical for better understanding the population of short gamma-ray bursts and their host galaxies. On the other hand, local-universe detections are excellent candidates for compact object mergers and thus gravitational wave event counterparts. With these results, we expect BlackCAT to contribute to exploring the early universe and assisting with the ever-growing field of multimessenger astronomy.

4.3 The Effect of Prompt vs. Extended Emission

In addition to simulating the full population of bursts (both with and without extended emission), further simulations were run to assess the case with extended emission present. In the full-population simulation, bursts with two-part light curves were run such that each corresponding region (prompt or extended) was scaled by its respective spectrum (cutoff power-law or simple power-law). For the collection of bursts with extended, two additional simulations were run: one with only the prompt region and one with only the extended region. This gives insight into BlackCAT's triggering method's sensitivity to the two types of emission.

Over the course of the 100-year simulation (corrected for the 76% duty cycle of BlackCAT), 257 bursts are found that contain both prompt and extended emission. 65 bursts are detected when looking at prompt emission alone. Simulating solely extended emission, 199 were successfully found. Comparing total light curve detection to prompt-only light curve detection suggests that the presence of extended emission increases the rate by a factor of ≈ 4. This is expected as BlackCAT is a soft X-ray instrument, looking primarily at lower energy photons. Because of the extended emission's typically softer spectra, we anticipate that BlackCAT should be more sensitive to this part of the light curve.

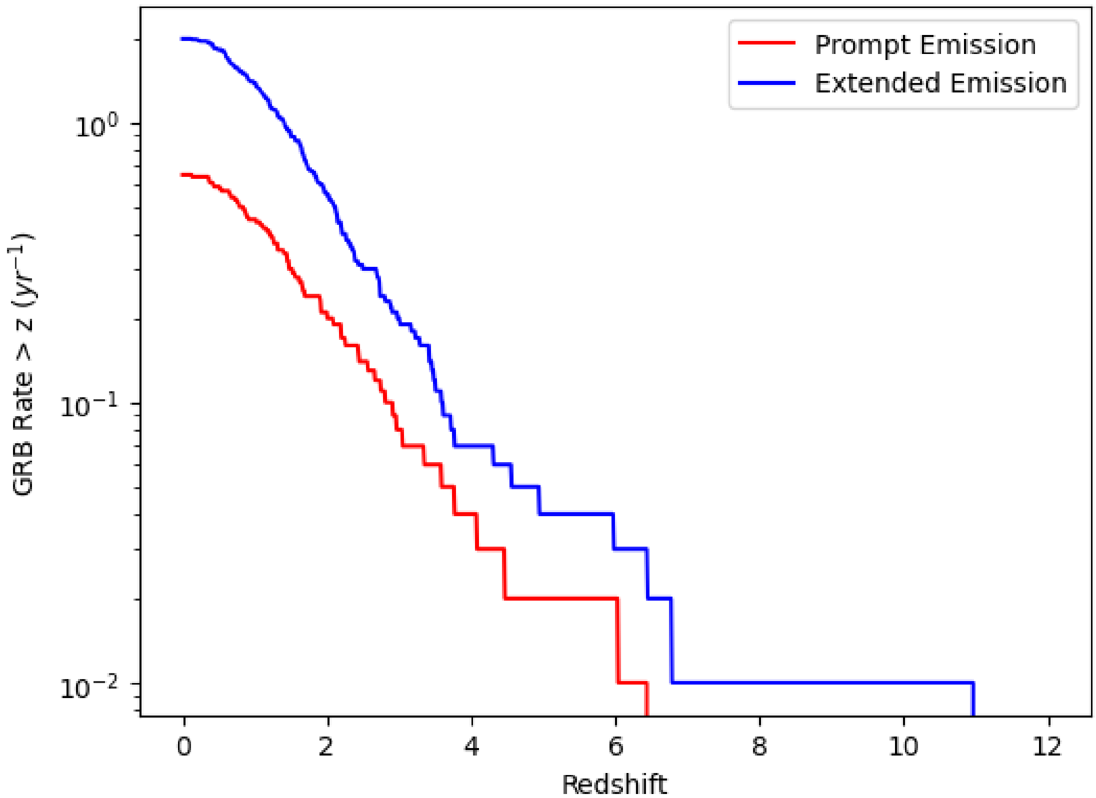

Figure 4.2: Shown is the cumulative detection rate above the threshold z. The population of bursts in this plot are only those with extended emission present. Plotted in blue is the cumulative detection rate for extended-only emission. Plotted in red is the cumulative detection rate for prompt-only emission.

Because of BlackCAT's increased sensitivity to extended emission, we should expect that its presence should impact the detected redshift population. Figure 4.2 shows the redshift distributions for prompt only and extended only in the collection of bursts where extended emission is present. As expected, we see an overall increased rate of detection across all redshifts for light curves containing solely extended emission as compared to solely prompt. Additionally, our results indicate that BlackCAT may be more sensitive to extended emission at very high redshifts, though the small sample size at these large values results in greater uncertainty in these regions.

Chapter 5

Conclusions

5.1 Conclusions and Future Work

Since initial observations of gamma-ray bursts, much work has been done to understand their physical properties and astronomical utility. The identification of GRB afterglows allowed for precise positioning and follow-up observation. Analysis of this data provided host galaxy identification, accurate redshifts, and supernova counterparts. Further work revealed a bimodal separation of the GRB population about the ~ 2 second duration. Long-soft bursts have been identified as collapsar-type events; short-hard bursts are most likely the result of compact object mergers. The likely progenitor of short gamma-ray bursts provides an exciting opportunity to use their observations to probe the most extreme environments in our universe via multimessenger astronomy. As gravitational wave counterparts, they promise insights into ultradense matter, General Relativity and strong gravity, r-process nucleosynthesis, and the cosmic expansion rate.

The BlackCAT instrument is a 6U CubeSat designed to search for high-redshift gamma-ray bursts in the soft X-ray band (0.5–20 keV). Utilizing a coded-aperture mask, we expect accurate sub-arcminute source localizations of $40''$ to $55''$ at 90%-confidence. With a wide FOV of 0.85 sr, BlackCAT will provide a significant catalog of well-positioned X-ray transient events. Its dawn-dusk Sun-synchronous orbit enables a persistent anti-Sun pointing, with detected transients generally well-laced for ground-based follow up observations.

We run a comprehensive set of simulations to test the detection sensitivity of BlackCAT to merger-type short gamma-ray bursts. To model the population of bursts, we sample light curves from the *Swift* BAT instrument. Where applicable, we make the distinction between the prompt and extended emission regions of the light curves. These have distinct spectral behavior, and fits are found to model this difference. The light curves are scaled to a redshift and luminosity taken from theoretical distributions provided by Ghirlanda et al. (2016). Integrating the redshift distribution over the cosmological volume integral (Wright, 2006), we find the expected rate of detectable bursts. A 100-year sample is generated and analyzed by testing the significance of 70 potential triggers of varying timescales within the BlackCAT sensitivity range. Scaling for point source and diffuse background via a BlackCAT pointing plan, we obtain successful detections.

Through our simulations, we find an expected detection rate of 2.8 short gamma-ray bursts per year across all redshifts. BlackCAT is designed to search for bursts in the high-redshift universe. Our results show that, given a long enough mission time, we may expect to see bursts out to $z \gtrsim 6$. In addition, we investigate the effect of prompt and extended emission on BlackCAT's sensitivity. We find that BlackCAT is more sensitive to extended emission across all redshifts, and the presence of extended emission may increase the potential redshift a burst can be seen from. This is expected, as extended emission has a notably softer spectrum, giving a better chance of being seen by BlackCAT's soft X-ray detectors.

Further investigations into the detection expectations for the high-redshift universe may prove useful. Because of the lower event probability at early times, our uncertainty begins to increase significantly beyond $z \approx 4$ for the 100-year simulation. A longer, dedicated simulation in the high-redshift regime may show more accurately what we expect for the detection of early mergers and the effect that prompt and extended emission may have on distant event sensitivity.

The successful launch of BlackCAT earlier this year is an exciting step in gamma-ray burst astronomy. High redshift detections of GRBs will prove valuable to characterizing the population of these high-energy events in the early universe. Accurate nearby burst detections will create opportunities for swift gravitational wave counterpart observations. The work resulting from this mission will shed light on some of the most extreme events in our universe and prove a useful tool for astrophysics, nuclear physics, and cosmology.

Bibliography

Abbott, B. P., Abbott, R., Adhikari, R., et al. 2009, Reports on Progress in Physics, 72, 076901, doi: http://doi.org/10.1088/0034-4885/72/7/07690110.1088/0034-4885/72/7/076901

Abbott, B. P., Abbott, R., Abbott, T. D., et al. 2016, , 93, 122003, doi: http://doi.org/10.1103/PhysRevD.93.12200310.1103/PhysRevD.93.122003

—. 2017a, , 119, 161101, doi: http://doi.org/10.1103/PhysRevLett.119.16110110.1103/PhysRevLett.119.161101

—. 2017b, , 848, L12, doi: http://doi.org/10.3847/2041-8213/aa91c910.3847/2041-8213/aa91c9

—. 2018, , 121, 161101, doi: http://doi.org/10.1103/PhysRevLett.121.16110110.1103/PhysRevLett.121.161101

—. 2021, , 909, 218, doi: http://doi.org/10.3847/1538-4357/abdcb710.3847/1538-4357/abdcb7

Abe, H., Akutsu, T., Ando, M., et al. 2022, Galaxies, 10, 63, doi: http://doi.org/10.3390/galaxies1003006310.3390/galaxies10030063

Accadia, T., Acernese, F., Alshourbagy, M., et al. 2012, Journal of Instrumentation, 7, 3012, doi: http://doi.org/10.1088/1748-0221/7/03/P0301210.1088/1748-0221/7/03/P03012

Acciari, V. A., Ansoldi, S., Antonelli, L. A., et al. 2021, , 908, 90, doi: http://doi.org/10.3847/1538-4357/abd24910.3847/1538-4357/abd249

Berger, E. 2014, , 52, 43, doi: http://doi.org/10.1146/annurev-astro-081913-03592610.1146/annurev-astro-081913-035926

Berger, E., Zauderer, B. A., Levan, A., et al. 2013, , 765, 121, doi: http://doi.org/10.1088/0004-637X/765/2/12110.1088/0004-637X/765/2/121

Bhat, P. N. 2010, GRB Coordinates Network, 10912, 1

—. 2011, GRB Coordinates Network, 11877, 1

Bissaldi, E., Meegan, C., Wood, J., & Fermi GBM Team. 2020, GRB Coordinates Network, 27543, 1

Boella, G., Butler, R. C., Perola, G. C., et al. 1997, , 122, 299, doi: http://doi.org/10.1051/aas:199713610.1051/aas:1997136

Colosimo, J. M., Fox, D. B., Falcone, A. D., et al. 2024, , 969, 138, doi: http://doi.org/10.3847/1538-4357/ad4f8b10.3847/1538-4357/ad4f8b

Comastri, A., Setti, G., Zamorani, G., & Hasinger, G. 1995, , 296, 1, doi: http://doi.org/10.48550/arXiv.astro-ph/940906710.48550/arXiv.astro-ph/9409067

Costa, E., Frontera, F., Heise, J., et al. 1997, , 387, 783, doi: http://doi.org/10.1038/4288510.1038/42885

Coulter, D. A., Foley, R. J., Kilpatrick, C. D., et al. 2017, Science, 358, 1556, doi: http://doi.org/10.1126/science.aap981110.1126/science.aap9811

D'Avanzo, P., Salvaterra, R., Bernardini, M. G., et al. 2014, , 442, 2342, doi: http://doi.org/10.1093/mnras/stu99410.1093/mnras/stu994

Eichler, D., Livio, M., Piran, T., & Schramm, D. N. 1989, , 340, 126, doi: http://doi.org/10.1038/340126a010.1038/340126a0

Evans, P. A., Cenko, S. B., Kennea, J. A., et al. 2017, Science, 358, 1565, doi: http://doi.org/10.1126/science.aap958010.1126/science.aap9580

Foley, S., & Meegan, C. 2013, GRB Coordinates Network, 15011, 1

Fong, W., Laskar, T., Rastinejad, J., et al. 2021, , 906, 127, doi: http://doi.org/10.3847/1538-4357/abc74a10.3847/1538-4357/abc74a

Fox, D. B., Frail, D. A., Price, P. A., et al. 2005, , 437, 845, doi: http://doi.org/10.1038/nature0418910.1038/nature04189

Frederiks, D., Golenetskii, S., Aptekar, R., et al. 2016a, GRB Coordinates Network, 19977, 1

—. 2016b, GRB Coordinates Network, 19288, 1

Galama, T. J., Vreeswijk, P. M., van Paradijs, J., et al. 1998, , 395, 670, doi: http://doi.org/10.1038/2715010.1038/27150

Gehrels, N., Chincarini, G., Giommi, P., et al. 2004, , 611, 1005, doi: http://doi.org/10.1086/42209110.1086/422091

Ghirlanda, G., Salafia, O. S., Pescalli, A., et al. 2016, , 594, A84, doi: http://doi.org/10.1051/0004-6361/20162899310.1051/0004-6361/201628993

Golenetskii, S., Aptekar, R., Frederiks, D., et al. 2010a, GRB Coordinates Network, 11470, 1

—. 2010b, GRB Coordinates Network, 11127, 1

Golenetskii, S., Aptekar, R., Mazets, E., et al. 2013, GRB Coordinates Network, 14668, 1

Golenetskii, S., Aptekar, R., Frederiks, D., et al. 2014, GRB Coordinates Network, 16868, 1

—. 2015, GRB Coordinates Network, 18226, 1

Hamburg, R., Malacaria, C., Meegan, C., & Fermi GBM Team. 2020, GRB Coordinates Network, 29140, 1

Hamburg, R., von Kienlin, A., & Meegan, C. 2018, GRB Coordinates Network, 23078, 1

Jin, Z. P., Yan, T., Fan, Y. Z., & Wei, D. M. 2007, , 656, L57, doi: http://doi.org/10.1086/51297110.1086/512971

Jordana-Mitjans, N., Mundell, C. G., Guidorzi, C., et al. 2022, VizieR Online Data Catalog: GRB 180618A light curves (Jordana-Mitjans+, 2022), VizieR Online Data Catalog: J/ApJ/939/106. Originally published in: 2022ApJ...939..106J, doi: http://doi.org/10.26093/cds/vizier.1939010610.26093/cds/vizier.19390106

Kalogera, V., Kim, C., Lorimer, D. R., et al. 2004, , 601, L179, doi: http://doi.org/10.1086/38215510.1086/382155

Kaneko, Y., Bostancı, Z. F., Göğüş, E., & Lin, L. 2015, , 452, 824, doi: http://doi.org/10.1093/mnras/stv128610.1093/mnras/stv1286

Kouveliotou, C., Meegan, C. A., Fishman, G. J., et al. 1993, , 413, L101, doi: http://doi.org/10.1086/18696910.1086/186969

Kozlova, A., Golenetskii, S., Aptekar, R., et al. 2017, GRB Coordinates Network, 21398, 1

Kulkarni, S. R., Frail, D. A., Wieringa, M. H., et al. 1998, , 395, 663, doi: http://doi.org/10.1038/2713910.1038/27139

Lamb, G. P., Lyman, J. D., Levan, A. J., et al. 2019, , 870, L15, doi: http://doi.org/10.3847/2041-8213/aaf96b10.3847/2041-8213/aaf96b

Leonov, A. A., Galper, A. M., Topchiev, N. P., et al. 2022, Advances in Space Research, 69, 514, doi: http://doi.org/10.1016/j.asr.2021.10.03110.1016/j.asr.2021.10.031

Levan, A. J., Tanvir, N. R., Starling, R. L. C., et al. 2014, , 781, 13, doi: http://doi.org/10.1088/0004-637X/781/1/1310.1088/0004-637X/781/1/13

Lien, A. Y., Barthelmy, S. D., Beardmore, A. P., et al. 2018, GRB Coordinates Network, 23047, 1

Lü, H.-J., Yuan, Y., Lan, L., et al. 2020, , 898, L6, doi: http://doi.org/10.3847/2041-8213/aba1ed10.3847/2041-8213/aba1ed

MacFadyen, A. I., & Woosley, S. E. 1999, , 524, 262, doi: http://doi.org/10.1086/30779010.1086/307790

Mailyan, B., Meegan, C., & Fermi GBM Team. 2019, GRB Coordinates Network, 26118, 1

Mangan, J., Dunwoody, R., Meegan, C., & Fermi GBM Team. 2021, GRB Coordinates Network, 31210, 1

Margutti, R., & Chornock, R. 2021, , 59, 155, doi: http://doi.org/10.1146/annurev-astro-112420-03074210.1146/annurev-astro-112420-030742

Margutti, R., Berger, E., Fong, W., et al. 2017, , 848, L20, doi: http://doi.org/10.3847/2041-8213/aa905710.3847/2041-8213/aa9057

Mazets, E. P., Golenetskii, S. V., Ilinskii, V. N., et al. 1981, , 80, 3, doi: http://doi.org/10.1007/BF0064914010.1007/BF00649140

McBreen, S. 2010, GRB Coordinates Network, 11489, 1

Meegan, C., Lichti, G., Bhat, P. N., et al. 2009, , 702, 791, doi: http://doi.org/10.1088/0004-637X/702/1/79110.1088/0004-637X/702/1/791

Meegan, C. A., Fishman, G. J., Wilson, R. B., et al. 1992, , 355, 143, doi: http://doi.org/10.1038/355143a010.1038/355143a0

Mészáros, P., & Rees, M. J. 1997, , 476, 232, doi: http://doi.org/10.1086/30362510.1086/303625

Metzger, B. D. 2020, Living Reviews in Relativity, 23, 1, doi: http://doi.org/10.1007/s41114-019-0024-010.1007/s41114-019-0024-0

Metzger, M. R., Djorgovski, S. G., Kulkarni, S. R., et al. 1997, , 387, 878, doi: http://doi.org/10.1038/4313210.1038/43132

Minaev, P., Pozanenko, A., & GRB IKI FuN. 2022, GRB Coordinates Network, 31566, 1

Moretti, A., Pagani, C., Cusumano, G., et al. 2009, , 493, 501, doi: http://doi.org/10.1051/0004-6361:20081119710.1051/0004-6361:200811197

Nakahira, S., Tsunemi, H., Tomida, H., et al. 2020, , 72, 17, doi: http://doi.org/10.1093/pasj/psz13910.1093/pasj/psz139

O'Connor, B., Troja, E., Dichiara, S., et al. 2021, , 502, 1279, doi: http://doi.org/10.1093/mnras/stab13210.1093/mnras/stab132

Paciesas, W. 2010, GRB Coordinates Network, 10345, 1

Paciesas, W. S., Meegan, C. A., Pendleton, G. N., et al. 1999, , 122, 465, doi: http://doi.org/10.1086/31322410.1086/313224

Paczynski, B. 1992, , 355, 521, doi: http://doi.org/10.1038/355521a010.1038/355521a0

Pizzichini, G., Ferrero, P., Gianotti, F., Morelli, E., & HETE Science Team. 2004, Memorie della Societa Astronomica Italiana Supplementi, 5, 166

Rau, A., Kienlin, A. V., Hurley, K., & Lichti, G. G. 2005, , 438, 1175, doi: http://doi.org/10.1051/0004-6361:2005315910.1051/0004-6361:20053159

Roberts, O. J. 2016, GRB Coordinates Network, 19265, 1

Roberts, O. J., & Hui, C. M. 2016, GRB Coordinates Network, 19289, 1

Rouco Escorial, A., Fong, W., Veres, P., et al. 2021, , 912, 95, doi: http://doi.org/10.3847/1538-4357/abee8510.3847/1538-4357/abee85

Sakamoto, T., Troja, E., Aoki, K., et al. 2013, , 766, 41, doi: http://doi.org/10.1088/0004-637X/766/1/4110.1088/0004-637X/766/1/41

Sakamoto, T., Barthelmy, S. D., Baumgartner, W. H., et al. 2014, GRB Coordinates Network, 16438, 1

Shan, Y., Liu, X., Yang, X., Yuan, H., & Lü, H. 2024, Research in Astronomy and Astrophysics, 24, 085003, doi: http://doi.org/10.1088/1674-4527/ad58a710.1088/1674-4527/ad58a7

Siegel, D. M. 2019, European Physical Journal A, 55, 203, doi: http://doi.org/10.1140/epja/i2019-12888-910.1140/epja/i2019-12888-9

Stanek, K. Z., Matheson, T., Garnavich, P. M., et al. 2003, , 591, L17, doi: http://doi.org/10.1086/37697610.1086/376976

Svinkin, D., Frederiks, D., Lysenko, A., et al. 2023, GRB Coordinates Network, 35079, 1

Swank, J. H. 1999, Nuclear Physics B Proceedings Supplements, 69, 12, doi: http://doi.org/10.1016/S0920-5632(98)00175-310.1016/S0920-5632(98)00175-3

Troja, E., King, A. R., O'Brien, P. T., Lyons, N., & Cusumano, G. 2008, , 385, L10, doi: http://doi.org/10.1111/j.1745-3933.2007.00421.x10.1111/j.1745-3933.2007.00421.x

Tsvetkova, A., Golenetskii, S., Aptekar, R., et al. 2017, GRB Coordinates Network, 21045, 1

van Paradijs, J., Groot, P. J., Galama, T., et al. 1997, , 386, 686, doi: http://doi.org/10.1038/386686a010.1038/386686a0

Veres, P., & Fermi-GBM Team. 2021, GRB Coordinates Network, 30540, 1

Veres, P., & Meegan, C. 2017, GRB Coordinates Network, 20551, 1

Villasenor, J. S., Lamb, D. Q., Ricker, G. R., et al. 2005, , 437, 855, doi: http://doi.org/10.1038/nature0421310.1038/nature04213

von Kienlin, A. 2010, GRB Coordinates Network, 10381, 1

von Kienlin, A., & Burns, E. 2015, GRB Coordinates Network, 17319, 1

von Kienlin, A., & Meegan, C. 2015, GRB Coordinates Network, 18756, 1

Woosley, S. E., & Bloom, J. S. 2006, , 44, 507, doi: http://doi.org/10.1146/annurev.astro.43.072103.15055810.1146/annurev.astro.43.072103.150558

Wright, E. L. 2006, , 118, 1711, doi: http://doi.org/10.1086/51010210.1086/510102

Yang, J., Ai, S., Zhang, B.-B., et al. 2022, , 612, 232, doi: http://doi.org/10.1038/s41586-022-05403-810.1038/s41586-022-05403-8

Luke Royer

lukeroyer625@gmail.com – (814) 933-7715

Permanent Address
315 Muhlenberg Ave.
Mount Gretna, PA 17064

EDUCATION

The Pennsylvania State University, University Park, PA — Expected Graduation Date: May 2026
Bachelor of Science in Astronomy and Astrophysics — Cumulative GPA: 4.00/4.00
Bachelor of Science in Physics — Dean's List
Schreyer Honors College
Eberly College of Science

SCIENTIFIC RESEARCH AND EDUCATIONAL EXPERIENCE

Research Assistant, *Penn State University* — Summer 2024 – Present

- Adapt Gamma Ray Burst simulation packages in Python to simulate 100 years of BlackCAT observations for preliminary detection estimates.
- Complete a literature review of over 50 articles to find values of Peak Energies for previously detected and analyzed Gamma Ray Bursts.
- Compile a database of 79 known Gamma Ray Bursts and relevant scientific values as a contribution to future research.

Learning Assistant, *Penn State University* — Spring 2024; Fall 2024 – Spring 2025

- Lead weekly office hours; provide an inclusive active learning environment.
- Develop teaching strategies for effective science communication and astrophysics education.
- Engage with students to provide personalized educational enrichment.
- Collaborate with professors to identify students' areas of difficulty.

RELEVANT COURSEWORK

Astronomy

- ASTRO 480 – Galaxies and Cosmology – Spring 2026
- ASTRO 485 – Introduction to High-Energy Astronomy – Fall 2025
- ASTRO 414 – Stellar Structure and Evolution – Fall 2025
- ASTRO 442 – Astrophysical Fluid Dynamics – Spring 2025
- ASTRO 320 – Observational Astronomy Laboratory – Fall 2024

Physics

- PHYS 458 – Intermediate Optics – Spring 2026
- PHYS 457 – Experimental Physics – Fall 2025
- PHYS 420 – Thermal Physics – Fall 2025
- PHYS 479 – Special and General Relativity – Spring 2025
- PHYS 410 – Introduction to Quantum Mechanics – Spring 2025
- PHYS 419 – Theoretical Mechanics – Fall 2024
- PHYS 400 – Intermediate Electricity and Magnetism – Fall 2024

Mathematics

- MATH 414 – Introduction to Probability Theory – Spring 2025
- MATH 417 – Qualitative Theory of Differential Equations – Spring 2024
- MATH 311 – Concepts of Discrete Mathematics – Spring 2024
- MATH 220 – Matrices – Summer 2023

AWARDS AND HONORS

- The Evan Pugh Scholar Senior Award
- The President Sparks Award
- The President Walker Award
- Schreyer Academic Excellence Scholarship
- Schreyer Honors College International Travel Grant
- Mercedes T. Richards Memorial Scholarship in Astronomy and Astrophysics
- The Bert Elsbach Honors Scholarship in Physics
- Eagle Scout and Order of the Arrow Member

ACTIVITIES AND ORGANIZATIONS

Pulsar Science Collaboratory, *President* Spring 2022 – Present

- Analyze radio data as prepfold and single pulse plots for the presence of pulsar candidates.
- Manage organization's finances to plan educational trips and execute merchandise sales.
- Educate members in science outreach and communication.
- Completed and passed the Mentor Certification course through NANOGrav.

Society of Physics Students, *Member* Fall 2022 – Present

- Attend regular meetings to develop a strong network of peers who share my interest in physics.

Study Abroad – The Culture of Deliberative Democracy in Ireland, *Student* Summer 2025

- Took honors-level course discussing the governmental and cultural functions of Ireland.
- Created a documentary investigating the effects of crisis on Irish politics.
- Worked with a group to thoroughly research Irish democracy.
- Interviewed citizens of different cultural backgrounds and perspectives.

Pride of the Lions Pep Band, *Member* Fall 2022 – Spring 2022

- Performed at college-level sporting events including Women's Volleyball, Men's Basketball, and Women's Basketball.
- Scheduled around the sporadic timing of sporting events.

SKILLS

Research Experience, Data Analysis Experience, Python Experience, Jupyter Notebook

Teamworking Skills, Efficient Workflow, Public Communication, Personable Leadership, Effective Educator